UC Santa Barbara

Title

Seasonality of California Central Coast Microseisms

Permalink

Authors

Shabtian, Hannah S
Eilon, Zachary C
Tanimoto, Toshiro

Publication Date

DOI

Copyright Information

Seasonality of California Central Coast Microseisms

Hannah S. Shabtian[*1,2] ![ORCID], Zachary C. Eilon[1] ![ORCID], and Toshiro Tanimoto[1] ![ORCID]

ABSTRACT

Linear scattering of ocean wave energy at the ocean–continent transition structure causes the primary microseism at a period of 14 s. Subsequent nonlinear wave–wave interactions produce the secondary microseism signal at half the primary microseism period (Longuet-Higgins, 1950; Haubrich et al., 1963). We use three years (2018–2022) of seismic data from an ongoing microarray deployment in the UC Santa Barbara Sedgwick Reserve, situated in the Santa Ynez Valley, to constrain seasonal and long-term microseismic noise characteristics for this portion of California's central coast. Ancillary buoy data (spectral data, wave height, wind speed and direction) from the National Oceanic and Atmospheric Administration are used to explore the causal relationship between ocean swell and the generation of microseisms. This region is found to exhibit strong seasonality in the primary and secondary microseism bands (0.05–0.1 and 0.1–0.3 Hz, respectively), with much higher noise levels in the winter compared with the summer, especially for the secondary microseism (15.4 dB). We also observe a systematic shift in the peak frequency of the secondary microseism between the winter (~ 0.14 Hz) and summer (~ 0.20 Hz) months, which may reflect a difference in sources of secondary microseisms between the two seasons. Local buoy wave height and spectral data are well correlated with seismic power spectra during times of incoming storm swell in winter, indicating locally generated microseisms along the central coast during this season.

KEY POINTS

- Coastal seismic stations and ocean-buoy power spectra exhibit strong seasonal amplitude covariation.
- Both low- and high-frequency locally generated secondary microseisms are observed year round.
- Quieting of the local sea state in the summer reveals distally sourced low-frequency secondary microseisms.

Supplemental Material

INTRODUCTION

Coupling between wind-generated ocean waves and the seafloor produces low-frequency seismic waves called microseisms (Hasselmann, 1963). These microseisms are stochastic in nature and entail propagating seismic energy, primarily in the form of surface waves (Behr et al., 2013). They occur in the 0.05–0.5 Hz (20–2 s) band with distinct, broad spectral peaks corresponding to several source mechanisms. Signals occurring between 0.05 and 0.1 Hz are predominantly caused by interactions between incoming ocean waves and the near-shore seafloor. Ocean gravity waves propagating at and interacting with the ocean–continent transition structure generate seismic signals in this frequency band (a process distinct from the generation of surf noise or waves crashing on a beach). This signal
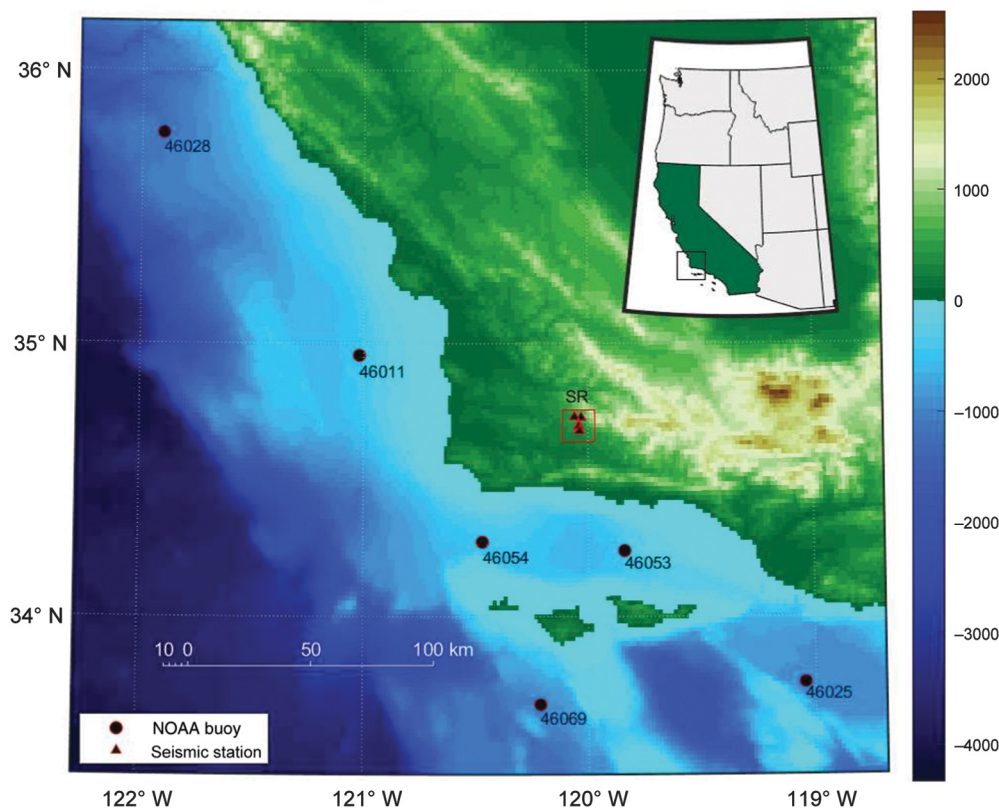
—called the primary microseism—has the same period as an incoming ocean swell (Haubrich et al., 1963). The secondary microseism, also called the double-frequency microseism, occurs at frequencies twice that of the primary microseism (0.1–0.25 Hz) and is caused by constructive interference between ocean gravity waves traveling in opposite directions. This interference results in standing gravity waves that cause pressure fluctuations at the seafloor that couple into the solid Earth, primarily producing Rayleigh waves with dominant energy at twice the frequency of the incoming ocean swell (Longuet-Higgins, 1950). This is sometimes termed low-frequency secondary microseism (LFSM) to distinguish it from another lower-energy, higher-frequency secondary microseism (HFSM) in the frequency band 0.25–0.5 Hz that may arise from local wind-induced wave interactions (Dorman et al.,

1. Department of Earth Science, University of California, Santa Barbara, Santa Barbara, California, U.S.A., ![ORCID] https://orcid.org/0009-0005-6129-5281 (HSS); ![ORCID] https://orcid.org/0000-0002-4373-646X (ZCE); ![ORCID] https://orcid.org/0000-0001-6980-5075 (TT); 2. Department of Earth, Environmental, and Planetary Sciences, Brown University, Providence, Rhode Island, U.S.A.

*Corresponding author: hannah_shabtian@brown.edu

Figure 1. Map of the California central coast, Sedgwick Reserve (SR) network (red box showing Sedgwick Reserve and triangles representing seismic stations), and National Oceanic and Atmospheric Administration buoys (black circles). The inset shows the study region with respect to the U.S. west coast. Elevation is given in meters.

SR network (see Fig. S1, available in the supplemental material to this article, for array configuration) and our study region. This reserve is situated far from any heavily trafficked roads, industrial machinery, and population centers and sees only light day use. This quiet noise environment is ideal for characterizing natural noise sources.

We use three-component (HHE, HHN, and HHZ) seismic data collected continuously from December 2018 to September 2022, recorded at 100 Hz. Instrument malfunctions resulted in a number of daily miniSEED files storing more than three traces. We ignore the data recorded these days.

Ocean wave data comes from the NOAA's National Data Buoy Center (NDBC). We use spectral and time-series data for ocean wave direction, speed, and height from the historical data of six buoys along the California coast for the years 2018–2022. These six buoys—46028, 46011, 46054, 46069, 46053, and 46025—are located in Cape San Martin, Santa Maria, West Santa Barbara, South Santa Rosa, East Santa Barbara, and Santa Monica basin, respectively (Fig. 1). We focus our discussion on the ocean wave height power spectral density (PSD; units of m^2/Hz) from these stations.

Buoy data are measured by a single-axis (perpendicular to the wave surface) accelerometer or inclinometer, which measure heave acceleration or vertical displacements, respectively. A fast Fourier transform is applied to the displacement or acceleration time series by a processor on board the buoys to produce the nondirectional spectral data. Response amplitude operator processing accounts for hull and electronic noise in the buoy spectral data. For detailed information about NOAA NDBC data processing, see Nondirectional and Directional Wave Analysis Procedures (Earle, 1996). Significant wave height (WVHT) is calculated as the average of the highest one-third of all wave heights during a 20 min sampling period and is reported by NOAA every hour. This dataset is temporally complete for the duration of our study period; we did not cull the buoy spectral or wave height data.

1993; Stephen *et al.*, 2003; Bromirski *et al.*, 2005; Zhang *et al.*, 2009; Ardhuin *et al.*, 2011; Cannata *et al.*, 2020).

This study aims to characterize the long-term variability and sources of the microseisms on the California central coast, expanding on other studies that have explored other parts of the California coast (e.g., Bromirski *et al.*, 1999; Gerstoft and Tanimoto, 2007). To understand the seasonal and yearly variability of the microseisms, we use three years (2018–2022) of ambient seismic noise data from a microarray deployed in a remote, low-noise environment north of Santa Barbara, California. These data are compared with local buoy data from National Oceanic and Atmospheric Administration (NOAA) buoys along the central coast to understand the generation of microseisms in this region. We discuss the temporal variability of ambient seismic noise and its source mechanisms in the central California coastal region, focusing primarily on secondary microseism sources and signals.

DATA

Seismic data for this study come from a microarray of one vault-enclosed and six direct-buried (~1 m depth) broadband seismometers in the Sedgwick Reserve (SR). This reserve is located in the Santa Ynez Valley, within the foothills of the San Rafael Mountains, Santa Barbara County, California. Figure 1 shows the

METHODS

Noisy waveforms are inherently stochastic. We focus on spectral analysis—both time-averaged and time-varying analyses—to characterize patterns in the microseisms. We compare seismic spectra to ocean wave spectra and wave height to understand the relationship between the oceans and seismic signals in our study region.

Seismic data

We subdivide daily seismic data into hourly time series, detrend the data, and remove instrument response (Beyreuther *et al.*, 2010). Welch's method (Welch, 1967) is used to estimate the PSD by segmenting each of the hourly time series, computing a periodogram for each segment, and then averaging the periodograms for the final PSD of the hour-long time series. The sampling frequency is 100 Hz. The segments are 1000 s long, tapered with a Hann window, and overlapped by 50%. We report one-sided spectra defined in the frequency range from 0.001 to 2 Hz, with units of $(m/s)^2/Hz$. All three seismic components (vertical, north, and east) are processed identically.

We take two approaches to examine long-term (monthly and seasonal) trends in the data. First, to examine coarse long-term trends, we stack PSDs over individual months of the year (e.g., summing all hourly spectra from the month of January for the years 2018 through 2022). Stacks are computed as the average PSD for all frequencies (0.001–2 Hz). These monthly stacks provide robust insight into seasonal changes by averaging over fluctuations on the scale of days and weeks and de-emphasize unusual seasons in any given year.

Second, to understand average site properties, we compute probability density functions (PDFs) of the PSDs (McNamara, 2004). These quantify the probability of a signal having a certain power at a given frequency over a specified time period. We use these PDFs to observe long-term station characteristics as well as to understand the key features of the ambient seismic spectrum in our study region.

We use PSD estimates from all available time windows to compute histograms of PSD values in octaves of frequency from 0.001 to 2 Hz and compute PSD PDFs for all three components at each station. Because the PDFs for all stations are similar (Figs. S8–S11), this study focuses on the results of station G3C1, which has the most complete dataset.

To assess short-term patterns in the seismic spectra, we compute the average PSD in distinct frequency bands (e.g., the secondary microseism, 0.1–0.3 Hz) and produce time series of these averaged PSDs for comparison with buoy wave height time series.

Buoy data

To elucidate seasonal and annual trends in the ocean wave spectrum, we use the same stacking methods as for the seismic data. These stacks are compared with the seismic stacks for similar time periods at frequencies of interest to explore quantitatively the coherency between the ambient ocean and seismic noise spectra. We also isolate average power in specific frequency bands to investigate how they vary and covary with seismic data over time.

RESULTS
### Seismic and buoy power spectra

The seismic PSD stacks (Fig. 2a) show two broad peaks near 0.06 and 0.14 Hz, corresponding to the primary (PM) and secondary (SM, specifically LFSM) microseisms, respectively. The secondary microseism has a higher and broader amplitude peak (−119 dB) than the primary (−140 dB) (also observed in the PSD PDFs; see Figs. S8–S11). The PDFs for all stations show the same trend and fall between the new low- and high-noise models (Peterson, 1993). The seismic spectra also show continued elevated noise levels in the HFSM 0.25–0.5 Hz frequency band.

Unlike the seismic spectrum, the ocean wave spectrum (Fig. 2b) has only one clear peak, at ∼0.06 Hz. (The frequency axis in Fig. 2b has been doubled to compare the amplitude modulation between the secondary microseismic signal and buoy data; in this figure, the peak appears at 0.12 Hz.) This is the frequency of wind-driven waves at the ocean surface and corresponds to the primary microseism signal. Both the seismic and buoy spectra see a shift in the frequency of the spectral maximum (for the secondary microseism, in the case of the seismic spectra) across different monthly averages, as well as a bifurcation of the spectral maximum in the "summer" (most obvious in July, August, and September) into a smaller amplitude peak at lower frequencies and a larger amplitude peak at higher frequencies.

Seasonality and seismic-buoy data correlation

Both the seismic- and ocean-buoy PSD estimates reflect strong seasonal variation in spectral amplitude (Fig. 2). Stacks of seismic PSD over individual months show that in the 0.05–0.25 Hz band, the winter months (December, January, and February) on average have the highest amplitude of noise (PM: −138.0 dB, SM: −115.2 dB) followed by the fall (September, October, and November; PM: −139.3 dB, SM: −115.3 dB) and spring (March, April, and May; PM: −140.4 dB, SM: −121.75 dB). The summer months have the lowest average noise levels (June, July, and August; PM: −141.0 dB, SM: −126.9 dB).

The seasonal variation is observed for both primary and secondary microseism frequencies, though there is a larger difference in noise level between the summer and winter months for the LFSM. For station G3C1, the difference between the highest and lowest amplitude primary microseism (i.e., highest winter vs. lowest summer noise level at ∼0.06 Hz from the monthly averages) is 4.69 dB. This corresponds to a five-fold
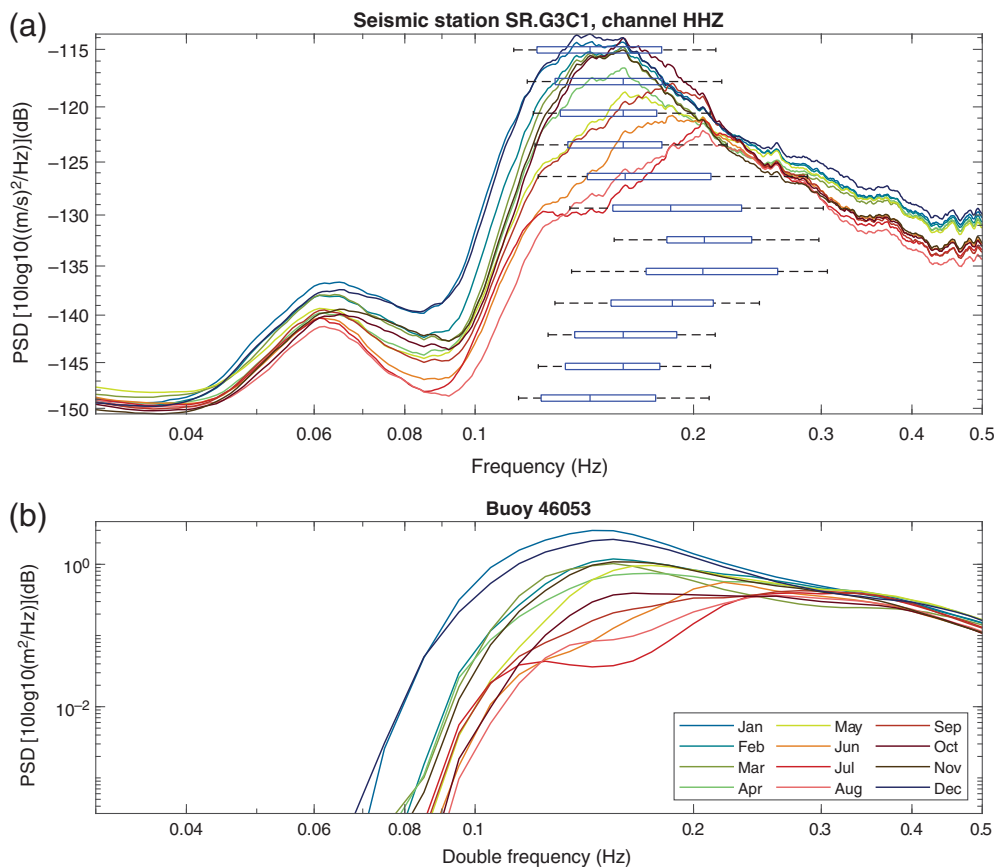
Figure 2. Power spectral density (PSD) stacks for the vertical component of (a) station G3C1 and (b) ocean buoy 46053. Colored lines represent a stack over individual months for all years of data collection. Box plots in panel (a) show the range of frequencies for which the highest 5% of the averaged seismic PSDs occur each month (January–December, from top to bottom). The frequency axis of buoy spectra in panel (b) is doubled for comparison with the seismic spectra in panel (a).
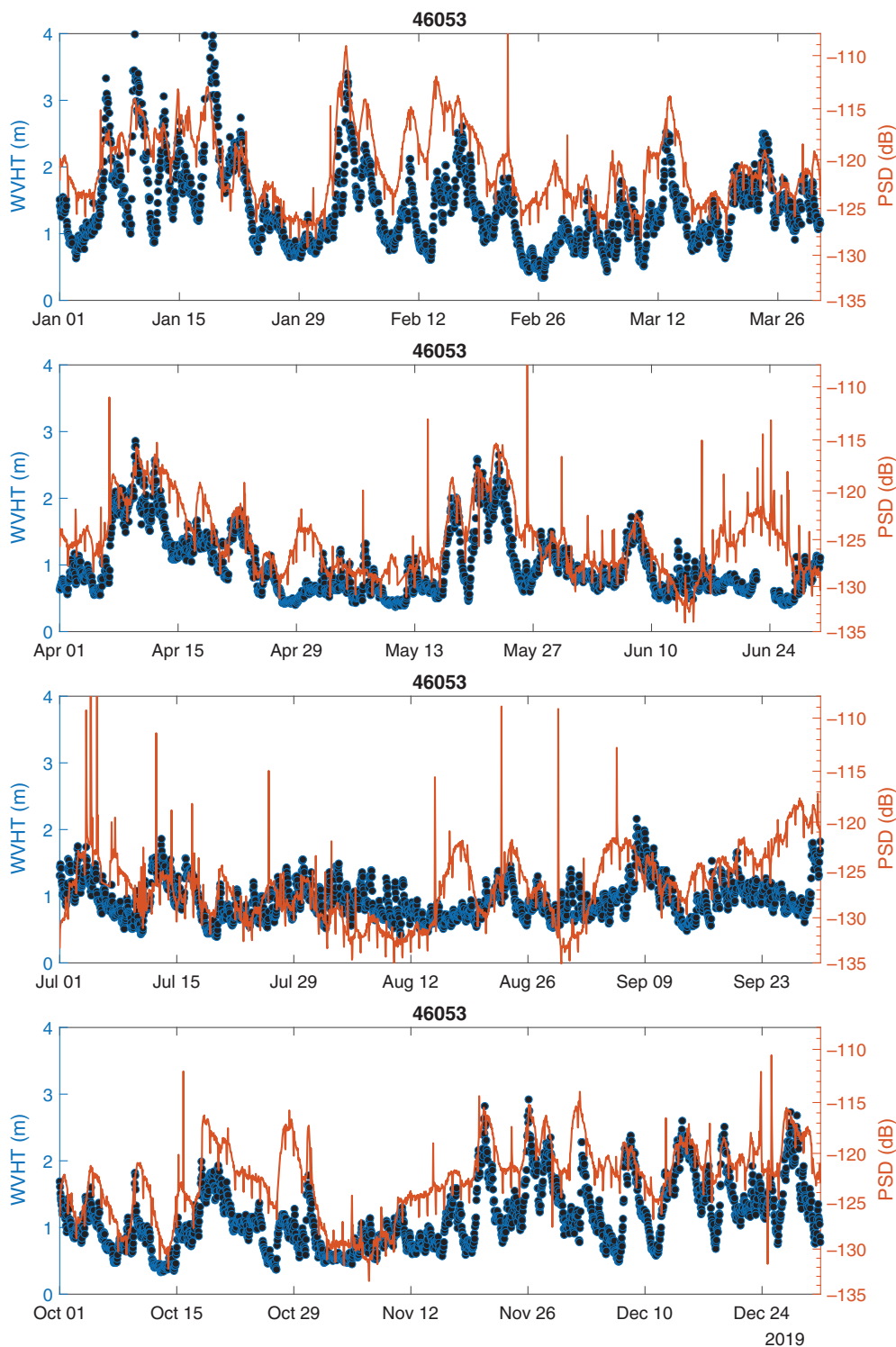
the band associated with the secondary microseism and has twice the frequency of the peak observed in the ocean wave spectra. Figure 3 shows the correspondence between WVHT buoy data and the secondary microseism PSD (i.e., averaged from 0.1 to 0.3 Hz) throughout 2019. Wave height and secondary microseism are strongly correlated from January until June. Although some long (>1 month) wavelength trends are distinct between the two datasets, the shorter (<2 weeks) variations are very closely related. Between mid-June and mid-September, we observe a low correlation. During this period, neither longer nor shorter variations in one time series are reflected in the other. The higher correlation resumes in mid-September and continues until the end of December.

Figure 4 quantifies this time-varying temporal correlation using a Pearson correlation coefficient computed for sliding 30-day windows centered on each day of the year 2019. Within each window, we remove the average from both time series but do not detrend. For all months except June, July, August, and September (summer months on the central coast), the computed correlation coefficient is generally >0.5. In the winter (January–March), the correlation is on average 0.72. In the summer (July–September), the correlation is on average 0.21.

DISCUSSION
Seasonality
The primary and secondary microseisms both display seasonal effects. As expected, we observe higher PSD both in the primary and secondary microseism bands in the winter months (December, January, February, and March) than in the summer months (June, July, August, and September) because of an increased storm presence and intensity during the Northern Hemisphere winter. The peak LFSM frequency also changes seasonally, shifting from lower frequencies (0.14 Hz) in the winter to higher frequencies (0.20 Hz) in the summer months. At the same time, very similar changes are observed in the local buoy wave spectra, albeit at double the period.

maximum average power difference between the two seasons. For the LFSM, the maximum difference between winter and summer noise levels is 15.4 dB.

In addition to seasonal changes in secondary microseism amplitude, we observe a change in the peak frequency of the LFSM. This is most obvious in the PSD stacks as a frequency shift between the LFSM peak (∼0.14 Hz) in the winter and spring months compared with the summer and fall months (∼0.20 Hz; box plots in Fig. 2a). In addition to this high-energy spectral maximum, we also see a smaller-amplitude peak LFSM signal with a frequency content of ∼0.12 Hz. We do not observe a change in the dominant frequency of the primary microseism.

Ocean waves exhibit similar seasonality to the microseisms, with winter PSD consistently higher than summer PSD (maximum difference of 2.9 dB) in the monthly stacks of Figure 2b.

We tested for similarity between temporal variations in WVHT and seismic PSD amplitude in several seismic frequency bands. We find that these two data types are most well correlated for the seismic frequency band 0.1–0.3 Hz. This is

Figure 3. PSD averages (G3C1) for 0.1–0.3 Hz plotted with buoy data for significant wave height (WVHT) (buoy 46053) for the year 2019. Time series are broken into three-month periods: January to March (top), April to June, July to September, and October to December (bottom).

low (0.21) in the summer. By contrast, if we evaluate the correlation between the same seismic noise variation and wave data from non-coastal buoys in the Pacific (Figs. S2 and S3), we see no such pattern. For instance, the correlation between wave height data from buoy 46059 (located 614 km from the nearest California coastline) and G3C1 microseisms is on average 0.45 during the winter (January–March) and 0.38 during the summer (July–September) in 2019. This provides some baseline for the relationship between seismic noise and more distal, open ocean noise sources. The maximum correlation is not nearly as high, and the seasonal pattern is much less strong (winter vs. summer differences in R are not statistically significant). We infer that the high correlation between local buoy wave height and secondary microseism in the winter is a direct result of seasonal wave energy locally delivered to the coast.

The transportable array (TA) in North America has been used to characterize variations in the microseismic spectrum before, with studies finding that the microseisms vary in power seasonally across the United States but are generally stable from year to year —agreeing with our results (Koper and Burlacu, 2015; Anthony et al., 2022). Using the TA, Koper and Burlacu (2015) did annual averaging of seismic power spectra, observing a splitting of the secondary microseism peak into

We find strong evidence that the seasonality of secondary microseism noise is directly related to highly local changes in sea state. The correlation between SM power and WVHT for local coastal buoy 46053 is very high in the winter (0.72) and

two periods, primarily in the western United States. They found covariance between the polarization and period of the secondary microseism, attributing this to geographical variation in microseism source areas and the ability of seismometers
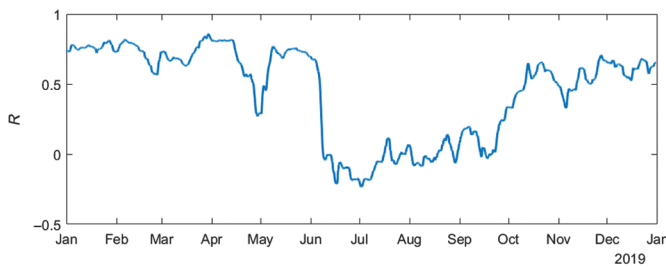
Figure 4. Correlation between secondary microseism power at station G3C1 with ocean wave height at buoy 46053. The Pearson correlation coefficient is computed using moving time windows of 30 days, and time series in each window are detrended.

to receive microseismic signals from more than one source location at a time (the Pacific and North Atlantic). In this study, we averaged the seismic PSD by month and did not see a double-peak secondary microseism in each monthly average. Instead, we saw a shift from one peak LFSM frequency in the winter (0.14 Hz) to two peak SM frequencies, one larger and one smaller (0.20 and 0.12 Hz, respectively), in the summer. This can be explained by the quieting of seismic noise during the summer months; because the local ocean waves produce lower amplitude microseisms in the summer, we are able to see the seismic signals coming from elsewhere—that is, signals that are not correlated with local ocean waves—in addition to the weaker local SM signals. Our results agree with other coastal studies of seismic noise, which were also able to distinguish between microseisms which are generated locally and distally (Becker *et al.*, 2020).

The shift in frequency of the peak secondary microseism energy, as well as the lack of correlation between local wave height and seismic PSD time series in July, August, and September, reflect differences in sources between summer and winter storm noise. Winter storm swells appear to generate more wave energy in the LFSM band locally, as seen by the good correspondence between the seismic PSD and local buoy data for WVHT for that half of the year. By contrast, the secondary microseismic signal from summer ocean swells (i.e., the secondary microseism recorded in the summer months) is not correlated with the local buoy data. The local ocean waves have not changed their frequency content, though, as one can see from the unchanged primary microseism peak frequency (Fig. 2).

Other local sources, such as wind, also do not seem to be producing particularly strong microseismic signals in this frequency band. Local wind energy as observed through local buoys is comparatively low during the summer (in accordance with the observed seasonality of local ocean wave energy), meaning that those local wind-driven seismic signals are not likely to cause the spectral maximum at 0.20 Hz. From this, we can infer that these higher-frequency LFSM signals are,

for the most part, not generated locally and are likely sourced from farther away (though there is always some local source contribution to the recorded microseisms, as seen by the presence of the 0.12 Hz peak in the bifurcated secondary microseism of the summer). We therefore interpret this shift in peak frequency of the LFSM as a quieting of the local sea state in the summer, allowing us to see more distal microseismic sources that are not well correlated with the local ocean waves. Although we only observe this spectral peak (0.20 Hz) in the summer, this source may exist year round and may be obscured by the much stronger local secondary microseism signals in the winter.

Because the seasonal differences in correlation between the secondary microseism and ocean WVHT are only observed locally, the generation of the secondary microseism is likely a primarily local phenomenon along the central coast—with the exception of the presence of the distal source observed in the summer.

Storm systems and microseism sources

The good correlation between local buoy wave height data and the secondary microseism amplitude in winter raises the possibility that we can use seismic data to track nearby storms during these months. Comparing seismic PSD and ocean wave height time series can tell us where storms impact first along the coast and how they move along the coast with time.

As an example, we focus on a Pacific storm that impacted the central coast between 13 and 20 January 2019 (Fig. 5). Ocean buoys measure wind and wavespeeds and directions, providing useful information about storm movement. For this storm, different buoys along the coast record the highest swells at different times, reflecting the areal extent and rate of motion of the storm system. We cross-correlate the time series of 0.1–0.3 Hz averaged PSD at G3C1 with the time series of wave heights at each buoy. On the timescale of a storm system's motion (km/day), seismic waves travel effectively instantaneously (km/s). If ocean waves at the locus of the storm's center produced equally detectable seismic waves wherever the storm was along its track, we would observe equally strong seismic noise throughout the storm's duration. This is not seen. Rather, we observe a negative, 9 hr lag between the seismic PSD (Fig. 5) and the wave height for the northmost buoy (46028—Cape San Martin). The highest waves (largest energy swells) arrive at this buoy before the seismic PSD maximum, consistent with the arrival of the storm swell from the north. At this point, the storm is either not generating significant seismic noise, or that noise is substantially attenuated on its way to our station. The storm then travels south-southwest (Figs. S5–S7) down the California coast, which is reflected by a diminishing lag between buoy and seismic data for signals at buoys 46011 (Santa Maria, 7 hr lag) and 46054 (West Santa Barbara, less than 2 hr lag), in that order. The ocean wave height and seismic PSD have zero lag (<1 hr) for 46069 (South Santa Rosa) and
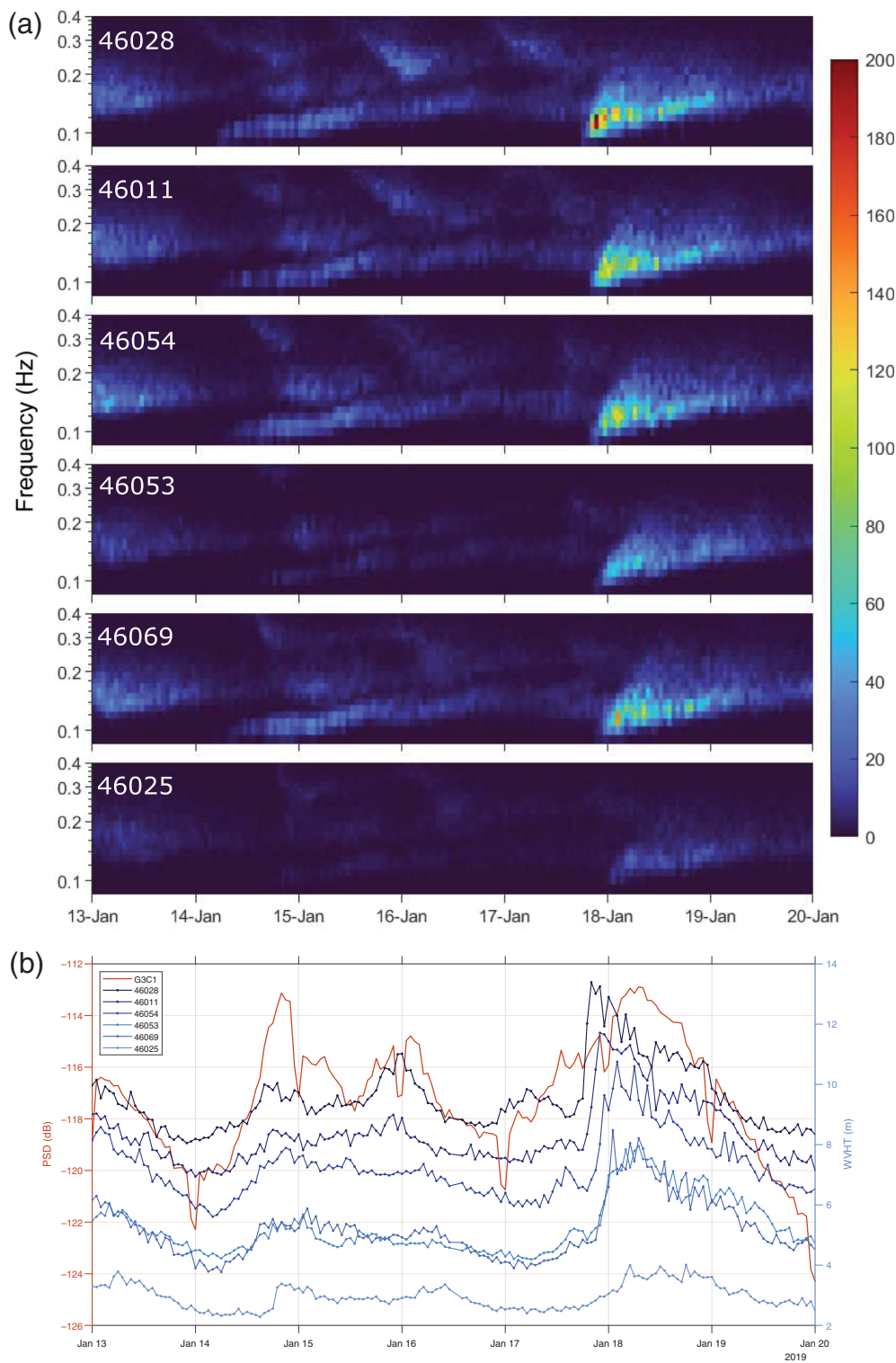
Figure 5. (a) Spectrograms from six central coast buoys for a storm during the week of 13–20 January 2019. The frequency axis on the buoy spectrograms has been doubled. (b) Seismic PSD averages (G3C1, orange line) for 0.1–0.3 Hz and WVHT measurements (blue lines) from the same six buoys. The wave height axis corresponds to buoy 46025, and other buoy WVHTs have their baselines shifted for clarity.

46053 (East Santa Barbara). This indicates that the seismic signals are most closely related to wave height in the particular region of these two buoys. This means that seismic noise generated at these locations is most clearly detected (due to maximally efficient coupling or minimal source–receiver attenuation) by our seismometers. Finally, a positive lag (the strongest seismic signal observed prior to the wave height maximum) of 6 hr is observed when the storm has traveled farther south to buoy 46025 (Santa Monica basin).

The lack of temporal lag between the seismic and buoy data for buoys 46069 and 46053 indicates that the secondary microseism recorded from our study region is being generated locally, within the region of the Channel Islands and Santa Barbara basin. This result confirms previous work on microseism generation near our study region (Bromirski, 2002; Gerstoft and Tanimoto, 2007; Tanimoto, 2007).

These locally generated secondary microseisms suggest that regional geography plays an important role in the generation of these seismic signals. Within our study region are the northern four Channel Islands, which are large land masses ~40 km south of the coastline nearest to our seismic array (Fig. 1). These islands break up and channelize swell to within the Santa Barbara basin. The south-facing coastline combined with the presence of the Channel Islands is likely a coastal geometry which is conducive to the constructive interference of ocean waves in such a fashion as

to yield strong secondary microseisms (Kimman *et al.*, 2012; Carvalho *et al.*, 2019).

Moving storms can also produce body waves in the microseismic frequency band (0.2–0.3 Hz). For especially fast storms, this energy is a significant component of the microseisms generated (Haubrich and McCamy, 1969). We cannot definitively distinguish between body and surface wave generation during this storm, but we observe (Fig. S4) the arrival of several more impulsive energy packets within the period of highest wave energy during the 13–20 January 2019 storm. These features, likely caused by wind–wave interaction, may indicate preferential body-wave generation during this time, though we cannot speculate on the causative mechanism.

The buoy and seismic spectrograms can further confirm coastal microseism generation by showing us the transfer of energy between the ocean waves and solid Earth occurring at the Channel Islands. These islands present a physical barrier to incoming storm swell. The higher power in the outermost buoys and much lower power in the innermost buoys, north of the Channel Islands (Fig. 5), indicates that wave energy is being blocked by the islands. We have presented evidence that this is also where ocean wave energy is being transferred into seismic waves.

Other features in both the buoy and seismic spectral data can illuminate the transfer of ocean waves to seismic energy. Dispersive effects are seen in both buoy and seismic spectral data and are most obvious during the highest-energy swells of the storm (18–20 January and 14–16 January) (Fig. 5 and Fig. S4, respectively).

High-energy features in the 0.2–0.5 Hz band of the seismic data (Fig. S4) that are not related to LFSM generation from the collision of ocean gravity waves from storms or their dispersive effects may be the result of wind-driven ocean wave interactions close to the coast. These higher-frequency features are also observed in the buoy spectral data. The three most prominent groups of peak energy in this band for the buoy data appear to align in time with three sudden increases in wind speed (Figs. S5–S7). These wind-generated microseisms exist within the frequency band of the HFSM and are features in the seismic spectra which are present year round, exhibiting the same seasonal behavior as the LFSM and primary microseism (Fig. 2a). The sharp features observed at around 0.07 Hz within the seismic spectral data are likely earthquakes.

A few studies have shown convincing evidence for wind-generated seismic noise on the ocean floor at frequencies above 0.3 Hz. They all show a good correlation between local wind data and seismic noise at high frequencies. In open oceans, examples include McCreery *et al.* (1993), whose work analyzed the Wake Island hydrophone array; Stephen *et al.* (2003) for the Ocean Seismic Network Pilot Experiment; and Bromirski *et al.* (2005) for the Hawaii-2 Observatory; and Duennebier *et al.* (2012) for the ALOHA Cabled Observatory. However, we know of no solely onland, near-coastal seismic data that have shown

wind-generated seismic noise. Our data clearly show the evidence of such high-frequency (≥0.3 Hz) seismic noise.

The single spectral peak observed in the buoy PSDs is much broader than the secondary microseism peak recorded by seismometers (Fig. 2). Moreover, although the shape of local buoy spectra changes seasonally largely in concert with that of the secondary microseism (shift in central frequency, change in overall amplitude, summer bifurcation into lower-*f* smaller and higher-*f* larger peaks), the range of frequencies over which this change manifests is smaller for the seismic spectrum. Because we have argued that the secondary microseism here is primarily locally generated, we can directly compare the shapes of the seismic and nearby buoy power spectra (doubling the buoy frequency scale to account for the wave interference effect). It seems that the transfer of ocean wave energy into seismic energy is band-limited. In particular, the PSD falloff going to higher frequencies is much more rapid for seismic data than for buoy data. Partly, this may result from attenuation, which (assuming frequency-independent Q) produces a spectral falloff proportional to *f*. It may also result from some sort of resonance or peak in the sensitivity of the coupling between seafloor pressure fluctuations and the solid Earth. More studies that directly tie local ocean wave properties to seismic noise are needed to explore this further.

CONCLUSION

Using three years (2018–2022) of ocean-buoy (NOAA) and ambient seismic (SR) data, we investigate seasonal variations in the primary and secondary microseism frequency seismic signals along the California central coast and the relationship between these seismic signals and ocean wave height.

We observe seasonal variations in the strength of the primary and secondary microseisms—the amplitudes of both signals being higher in the winter months than in the summer. We also observe a shift in the frequency of the LFSM peak energy toward higher frequencies (0.20 Hz) in the summer months compared than in the winter (0.14 Hz). There is a seasonally varying correlation between the secondary microseism and ocean wave height measured from local buoys, with a highly significant (0.72) correlation in the winter and essentially no correlation in the summer. We explain this as a shift in location and strength of noise sources; during the winter months, coastal storm swell locally generates noise, while diffuse and distal noise sources dominate in the summer.

Other coastal phenomena, such as local wind patterns within the Santa Barbara basin, may also explain higher-frequency seismic noise not directly associated with storm swell. These microseisms, with frequency content ≥0.3 Hz, are wind-driven HFSMs and are present throughout the year.

DATA AND RESOURCES

Ocean-buoy data from the National Oceanic and Atmospheric Administration can be accessed online at the National Data Buoy

DECLARATION OF COMPETING INTERESTS

The authors declare no competing interests.

REFERENCES

Anthony, R. E., A. T. Ringler, and D. C. Wilson (2022). Seismic background noise levels across the continental United States from USArray Transportable Array: The influence of geology and geography, *Bull. Seismol. Soc. Am.* **112,** no. 2, 646–668.

Ardhuin, F., E. Stutzmann, M. Schimmel, and A. Mangeney (2011). Ocean wave sources of seismic noise, *J. Geophys. Res.* **116** doi: 10.1029/2011JC006952.

Becker, D., L. Cristiano, J. Peikert, T. Kruse, F. Dethof, C. Hadziioannou, and T. Meier (2020). Temporal modulation of the local microseism in the North Sea, *J. Geophys. Res.* **125,** no. 10, e2020JB019770.

Behr, Y., J. Townend, M. Bowen, L. Carter, R. Gorman, L. Brooks, and S. Bannister (2013). Source directionality of ambient seismic noise inferred from three-component beamforming, *J. Geophys. Res.* **118,** 240–248.

Beyreuther, M., R. Barsch, L. Krischer, T. Megies, Y. Behr, and J. Wassermann (2010). ObsPy: A python toolbox for seismology, *Seismol. Res. Lett.* **81,** 530–533.

Bromirski, P. D. (2002). The near-coastal microseism spectrum: Spatial and temporal wave climate relationships, *J. Geophys. Res.* **107,** no. B8, 2166.

Bromirski, P. D., F. K. Duennebier, and R. A. Stephen (2005). Mid-ocean microseisms, *Geochem. Geophys. Geosyst.* **6,** no. 4 doi: 10.1029/2004GC000768.

Bromirski, P. D., R. E. Flick, and N. Graham (1999). Ocean wave height determined from inland seismometer data: Implications for investigating wave climate changes in the NE Pacific, *J. Geophys. Res. Oceans* **104,** no. C9, 20,753–20,766.

Cannata, A., F. Cannavò, S. Moschella, G. Di Grazia, G. Nardone, A. Orasi, M. Picone, M. Ferla, and S. Gresta (2020). Unravelling the relationship between microseisms and spatial distribution of sea wave height by statistical and machine learning approaches, *Rem. Sens.* **12,** no. 5, 761.

Carvalho, J. F., G. Silveira, M. Schimmel, and E. Stutzmann (2019). Characterization of microseismic noise in Cape Verde, *Bull. Seismol. Soc. Am.* **109,** no. 3, 1099–1109.

Dorman, L. M., A. E. Schreiner, L. D. Bibee, and J. A. Hildebrand (1993). Deep-water sea-floor array observations of seismo-acoustic noise in the eastern Pacific and comparisons with wind and swell, in *Natural Physical Sources of Underwater Sound*, B. R. Kerman (Editor), Kluwer Academic Publishers, Netherlands, 165–174.

Duennebier, F. K., R. Lukas, E.-M. Nosal, J. Aucan, and R. A. Weller (2012). Wind, waves, and acoustic background levels at station aloha, *J. Geophys. Res. Oceans* **117,** no. C3, doi: 10.1029/2011JC007267.

Earle, M. D. (1996). Nondirectional and directional wave data analysis procedures, NDBC Technical Document 96-01, 780 pp.

Gerstoft, P., and T. Tanimoto (2007). A year of microseisms in southern California, *Geophys. Res. Lett.* **34,** no. 20, L20304.

Hasselmann, K. (1963). A statistical analysis of the generation of microseisms, *Rev. Geophys.* **1,** no. 2, 177.

Haubrich, R. A., and K. McCamy (1969). Microseisms: Coastal and pelagic sources, *Rev. Geophys.* **7,** no. 3, 539.

Haubrich, R. A., W. H. Munk, and F. E. Snodgrass (1963). Comparative spectra of microseisms and swell, *Bull. Seismol. Soc. Am.* **53,** no. 1, 27–37.

Kimman, W. P., X. Campman, and J. Trampert (2012). Characteristics of seismic noise: Fundamental and higher mode energy observed in the northeast of the Netherlands, *Bull. Seismol. Soc. Am.* **102,** no. 4, 1388–1399.

Koper, K. D., and R. Burlacu (2015). The fine structure of double-frequency microseisms recorded by seismometers in North America, *J. Geophys. Res.* **120,** 1677–1691.

Longuet-Higgins, M. S. (1950). A theory of the origin of microseisms, *Philos. Trans. Royal Soc. A* **243,** no. 857, 1–35.

McCreery, C. S., F. K. Duennebier, and G. H. Sutton (1993). Correlation of deep ocean noise (0.4–30 Hz) with wind, and the holu spectrum—A worldwide constant, *J. Acoust. Soc. Am.* **93,** no. 5, 2639–2648.

McNamara, D. E. (2004). Ambient noise levels in the continental United States, *Bull. Seismol. Soc. Am.* **94,** no. 4, 1517–1527.

Peterson, J. (1993). *Observations and modeling of seismic background noise*, U.S. Department of Interior Geological Survey.

Stephen, R. A., F. N. Spiess, J. A. Collins, J. A. Hildebrand, J. Orcutt, K. R. Peal, F. L. Vernon, and F. B. Wooding (2003). Ocean Seismic Network Pilot Experiment, *Geochem. Geophys. Geosyst.* **4,** no. 10, doi: 10.1029/2002GC000485.

Tanimoto, T. (2007). Excitation of microseisms: Microseism excitation, *Geophys. Res. Lett.* **34,** no. 5, L05308, doi: 10.1029/2006GL029046.

Welch, P. (1967). The use of fast Fourier transform for the estimation of power spectra: A method based on time averaging over short, modified periodograms, *IEEE Trans. Audio Electroacoust.* **15,** no. 2, 70–73.

Zhang, J., P. Gerstoft, and P. M. Shearer (2009). High-frequency P-wave seismic noise driven by ocean winds, *Geophys. Res. Lett.* **36,** no. 9, L09302.